Energy Advances

ROYAL SOCIETY OF CHEMISTRY

PAPER

View Article Online
View Journal | View Issue

Cite this: *Energy Adv.*, 2023, 2, 1926

SnO_2/h-BN nanocomposite modified separator as a high-efficiency polysulfide trap in lithium–sulfur batteries†

Chandra Sekhar Bongu,[a] Yasmin Mussa,[a] Sara Aleid,[a] Muhammad Arsalan[b] and Edreese H. Alsharaeh *[a]

Received 8th June 2023,
Accepted 22nd September 2023

DOI: 10.1039/d3ya00260h

rsc.li/energy-advances

Lithium–sulfur batteries are one of the most promising alternatives to traditional lithium-ion batteries because of their exceptionally high theoretical energy density and low cost. However, the weak electrical conductivity of sulfur and capacity deterioration brought on by the shuttle effect of lithium polysulfides (LiPSs) limit the practical applications of Li–S batteries. Herein, we propose an efficient approach of using a two-dimensional material (h-BN) composite with SnO_2 in the separator to inhibit the mass transport of polysulfides from the cathode and subsequent parasitic reactions on the metallic lithium anode. The optimum concentration of 10 wt% h-BN was found to be sufficient to form SnO_2/h-BN with improved electrochemical behavior and induce a rapid conversion of trapped polysulfides. As a result, Li–S batteries with a separator modified with SnO_2/10% h-BN showed an improved specific capacity of 620 mA h g^{-1} at 1C, which was maintained at 485 mA h g^{-1} with a coulombic efficiency of 99% after 350 cycles. Furthermore, self-discharge studies suggest the feasibility of a modified separator for commercial applications.

1. Introduction

In recent years, lithium-ion batteries (LIBs) have been employed for mobile devices, large-scale energy storage, and electric vehicles. But conventional LIBs are unable to meet the increasing demand since they have almost hit their theoretical energy densities. Advanced rechargeable batteries with lower prices and greater energy densities are desperately needed. In this regard, lithium–sulfur batteries with a high theoretical energy density of 2600 W h kg^{-1}, high capacity (~1672 mA h g^{-1}), low cost, and benign raw material composition have long been seen to be one of the most potential candidates to replace LIBs.[1,2] However, the low usage, severe self-discharge, and short cycling life of LSBs substantially hinder their commercialization.[2–4] The insulating properties of sulfur (5×10^{-30} S cm^{-1} at 25 °C) limit the electrochemical activity, but the poor cyclability and low coulombic efficiency are mostly related to the loss of the active material. As an LSB discharges normally, solid sulfur (S_8) is converted into soluble lithium polysulfide (LiPS; Li_2S_x; x = 4–8) intermediates that can permeate through the electrolyte and settle on top of the anode, a process known as shuttling. Additional reduction processes on top of the anode may result from this shuttling of LiPS between the cathode and the anode. Due to active sulfur loss and high cell impedance caused by these short-range LiPSs on top of the anode, there is severe capacity degradation and low sulfur utilization.[5–8]

The most popular method for addressing these problems is to alter the cathode structure by enclosing sulfur in porous or hollow materials like carbon (such as hollow carbon, mesoporous carbon, carbon nanotubes, graphene, and graphene oxide).[9–15] These changed designs can prevent polysulfide diffusion to the anode by providing a physical barrier in addition to improving the sulfur cathode's electronic conductivity. Despite this, sulfur particles experience significant volumetric expansion following lithiation, which reduces the impact of structural changes over prolonged charging/discharging cycles. As a result, the focus of research has changed from cathode modification to separator modification.[16]

An electronic insulator called a separator is a membrane that keeps the anode and cathode from short-circuiting. Normal porous polymers are the membranes used in LIBs on a regular basis; they have no effect on how lithium ions are transported. However, the LiPSs might migrate to the anode through the separator's pores during the normal discharge of an LSB, leading to the shuttling phenomenon.[17] Because

[a] College of Science and General Studies, AlFaisal University, PO Box 50927, Riyadh, 11533, Saudi Arabia. E-mail: ealsharaeh@alfaisal.edu
[b] EXPEC Advanced Research Center, Saudi Aramco, P.O. Box 5000, Dhahran, 31311, Saudi Arabia

† Electronic supplementary information (ESI) available. See DOI: https://doi.org/10.1039/d3ya00260h

improved cathode designs have a limited impact due to sulfur's volume expansion problem, altering the separator is an alternative approach to reduce polysulfide shuttling in LSBs. The separators have been modified to improve the conductive layer and trap polysulfides using conductive carbon and polymers.[18–29] To take advantage of their potent interaction with polysulfides, metal oxides have been coated onto the polypropylene membrane separator.[30–35]

However, the majority of the metal oxides must be prepared using time-consuming procedures in challenging environments at a significant cost. SnO_2 is one of the metal oxides that has the advantages of being naturally abundant, less toxic and simple to produce. The separator functionalized with SnO_2 offers an effective approach to control the polysulfides.[36] Jing Liu *et al.*'s group found that SnO_2 nanoparticles coated on the polypropylene separator can significantly prevent the dissolution/diffusion of intermediate polysulfides and improve the electrochemical performance.[37] In order to suppress the polysulfide shuttle effect and improve the electrochemical reaction kinetics for cycling performance and rate capability, Hyunwoo Ahn *et al.* developed a multifunctional SnO_2-nanowires/carbon composite interlayer that can both adsorb lithium polysulfides and offer electron-conductive pathways to the sulfur electrode.[38]

Boron nitride (h-BN) nanosheets have attractive characteristics as a separator due to their properties as an insulator and being more stable chemically and electrochemically than other two-dimensional materials.[39,40] Boron nitride's combined sp^2 hybridized Lewis acid and Lewis base (boron atoms and nitrogen atoms) give it a distinctive property that makes it easy to interact with polysulfide species. A lone pair of electrons on nitrogen has the power to attract the positive end of the polysulfide species, and boron atoms in BN have a strong propensity to accept electron pairs from anion molecules (lithium).

In this study, we built a trapper for LiPSs in LSBs using a straightforward technique to design a heterostructure SnO_2 nanoparticle/h-BN modified separator. Strong chemical interactions between LiPSs and the SnO_2 nanoparticle/h-BN modified separator are visible. We demonstrate improved wettability, electrolyte absorption, and good stability at high temperatures for the SnO_2 nanoparticle/h-BN modified separator. Surprisingly, at room temperature, the SnO_2 nanoparticle/h-BN modified separator exhibits good half-cell LSB rate performance and cycling performance.

2. Experimental section

2.1. Synthesis of SnO_2 nanoparticles

A hydrothermal method was used to synthesize SnO_2 nanoparticles. The $SnCl_4$ precursor was mixed with absolute ethanol in the ratio of 1 : 5 (v/v ratio) and stirred for 1 hour to form a stable and clear solution at room temperature. To the above solution, ammonium hydroxide (NH_3OH) was added in the ratio of 2 : 3 (v/v) and stirred to yield a white precipitate. This mixed milky solution was transferred into a Teflon-lined stainless-steel autoclave and heated to 180 °C and 200 psi for 20 minutes holding time at a power of 1800 W in the microwave. After the reaction, the precipitate was collected and washed with distilled water and absolute ethanol several times and then left to dry at 80 °C in the oven overnight. After drying, the precipitate was calcined at 600 °C for 2 hours to obtain SnO_2 powder and to remove any excess reagents.

2.2. Functionalization of hexagonal boron nitride (h-BN)

In a typical synthesis, h-BN (100–150 mg) was added to 1 : 3 HNO_3/H_2SO_4, and the mixture was ultrasonically mixed for 2 hours and then N_2H_4 and hydrogen peroxide were added. The above solution was transferred into a Teflon-lined stainless-steel autoclave and heated to 80 °C for 2 hours. After the reaction, the solution was collected by filtration on a glass filter paper and washed with distilled water and absolute ethanol several times and then left to dry in the oven overnight. The solid phase was filtered on a glass filter, washed with water and acetone several times, and dried at room temperature to give a constant mass. The mass change of the sample upon functionalization was evaluated from the material balance.

2.3. Synthesis of SnO_2/h-BN nanocomposites

Different percentages of uncalcined SnO_2 were mixed with a solution of 100% pure ethanol and then sonicated for 1 hour. The mixture was then added to functionalized h-BN (2 mg mL^{-1}) that was sonicated for 1 hour. The prepared composites and the synthesis conditions are summarized in Table 1. The prepared composites were placed in the CEM (micro-oven) and the reaction conditions were set to 180 °C and 200 psi for 20 minutes holding time at a power of 1800 W. The precipitates were washed four times using 70% ethanol and then left to dry at 80 °C in the oven overnight. After drying, the nanocomposites were calcined at 600 °C for 2 hours to obtain SnO_2/h-BN powder and remove any excess reagents.

2.4. Preparation of the SnO_2/h-BN coated separator

The SnO_2/h-BN-modified separator was made using a straightforward slurry casting technique with a doctor blade. A slurry was created by dispersing a blend of SnO_2/h-BN, Super P carbon, and polyvinylidene fluoride (PVDF) in NMP solvent at a weight ratio of 80 : 10 : 10. With a doctor blade, the resultant slurry was cast onto one side of a commercial polypropylene separator (Celgard) at a thickness of 100 μm. The slurry-cast separator was dried in a vacuum oven overnight at 60 °C. The dried SnO_2/h-BN modified separator was then shaped into a 19 mm-diameter disk. The same procedure was used to prepare the SnO_2 and h-BN coated separator.

Table 1 Summary of the preparation of different composites

	h-BN (mL)	SnO_2 (mg)	Ethanol (mL)
SnO_2/5% h-BN	7.5	275	42.5
SnO_2/10% h-BN	15	270	35
SnO_2/25% h-BN	37.5	225	12.5

2.5. Preparation of the pure sulfur cathode

The cathode was constructed from 80% sulfur, 10% polyvinylidene difluoride binder (PVDF), and 10% super P conductive agent. The cathode materials were first thoroughly mixed in a solution of 1-methyl-2-pyrrolidinone (NMP) and then the slurry cast onto aluminum foil by using a doctor blade-coating technique. The electrode was punched into round discs with 15 mm diameter after being dried at 60 °C for 24 hours. The total sulfur content in the cathode is ~ 2 mg_{sulfur} cm^{-2}.

2.6. Synthesis of Li_2S_6 for adsorption studies

Li_2S and S_8 were used to prepare the 0.5 M Li_2S_6 solution in accordance with the reaction's stoichiometry coefficient: $Li_2S + (5/8)\ S_8 \rightarrow Li_2S_6$. In a thorough method, Li_2S (0.7g) and S_8 (0.3 g) were added to a mixed solvent of equal volume of 1,3-dioxolane (DOL) and 1,2-dimethoxyethane (DME). At 60 °C, the mixture was stirred for 48 hours. Before the adsorption test, it was diluted three times using a mixed solvent of equal volume of DOL and DME. All procedures were carried out inside the glove box, which was kept at an ambient air pressure of Ar atmosphere (H_2O 0.5 ppm, O_2 0.5 ppm).

2.7. Adsorption test with the sealed vial

The adsorption test of the polysulfides was carried out in closed bottles. The upper side of the bottle was filled with Li_2S_6 solution in a mixed solvent of 1,3-dioxolane (DOL) and 1,2-dimethoxyethane (DME), while the bottom side was filled with only a mixed solvent of DOL and DME. At the junction of the top and bottom of the bottle, the composite coated separator was inserted, and the diffusion of Li_2S_6 was monitored with time. The diffusion of polysulfides (Li_2S_6) was monitored for 24 hours inside the glove box.

3. Physical characterization

The morphology of the samples was characterized by scanning electron microscopy (SEM), transmission electron microscopy (TEM) and high-resolution transmission electron microscopy (HRTEM) by using FEI Quanta 200 and TEM, JEOL2100 Instruments. For sample preparation, the powder composite sample was dispersed in the ethanol–water mixture by 20 min ultrasonication followed by drop-casting onto a fresh lacey carbon copper grid. X-Ray diffraction (Rigaku Minflex 600) was used to study the crystallinity of the materials. Raman spectra of the samples were collected using a WITec Apyron Raman spectrometer and a 532 nm solid-state laser as the excitation source.

4. Electrochemical characterization

Slurry coating was used to prepare the sulfur cathodes. In order to create a homogeneous slurry, 80 weight percent sublimed sulfur, 10 weight percent carbon black, and 10 weight percent PVDF binder were disseminated in *N*-methyl-2-pyrrolidone (NMP). The slurry was then cast onto a current collector made of aluminum foil, and it was vacuum dried at 60 °C overnight. A glovebox (H_2O 0.5 ppm, O_2 0.5 ppm, MBraun, Unilab) filled with high-purity argon was used to assemble CR-2032-coin cells. Lithium foil was used as the reference/counter electrode (diameter: 15 mm and thickness: 0.5 mm) and a SnO_2/h-BN modified PP membrane (Celgard 2400) served as the separator. The employed electrolyte contained 1.0 wt% of $LiNO_3$ and was made up of 1,2-dimethoxyethane (DMC) and 1,3-dioxolane (DOL) in a volume ratio of 1 : 1. It also contained 1 M LiTFSI. The SnO_2, h-BN and SnO_2/h-BN-composite coated separators were placed into the cells with the functional interlayer facing the sulfur cathode. For comparison, a commercial polypropylene separator was used as the pristine separator. Using a Gamry electrochemical work station, data on galvanostatic charge–discharge and cycling were gathered over a voltage range of 1.8 to 3.0 V at room temperature. Electrical impedance spectroscopy (EIS) was performed between the frequencies of 0.01 and 100 kHz with an AC voltage amplitude of 5 mV s^{-1}. At a scan rate of 0.1 mV s^{-1}, CV measurements were made in the potential range of 1.8–3.0 V (*versus* Li/Li^+). Based on the sulfur mass, the specific capacities of the LSBs were computed.

5. Results and discussion

5.1. Physical characterization

By using X-ray diffraction (XRD) analysis, the crystalline phase of SnO_2 and SnO_2/h-BN composites was studied. In Fig. 1, the X-ray diffraction (XRD) patterns of SnO_2 and SnO_2/h-BN composites are displayed. The diffraction peaks of SnO_2 are shown in Fig. 1a, and according to JCPDS card no. 21-1250, all of the peaks can be indexed to the tetragonal structure. Since there are no impurity peaks visible, it is clear that the synthesis produced high purity SnO_2 nanoparticles. The h-BN powder XRD pattern is shown in Fig. 1b, and it remarkably resembles the JCPDS card no. 85–1068. The XRD patterns of SnO_2/h-BN composite products are shown in Fig. 1c–e, and the presence of strong, sharp peaks indicates that the final product is crystalline. Compared to the pristine SnO_2 and h-BN, the composites' peaks are shifted to the right side. The existence of the (002) peak at about 26.5°, indicating the interlayer spacing of h-BN, suggests homogeneous mixing of the composites. However, SnO_2/10% h-BN composites exhibit slightly broader Bragg peaks compared to the remaining two composites, thus indicating the nanocrystalline product formation, aided by the presence of more h-BN in the composite. In addition, the structure of the SnO_2/10% h-BN composite was characterized by Raman spectroscopy (Fig. S1, ESI†). The Raman spectra of SnO_2/10% h-BN in Fig. S1 (ESI†) inset shows three bands at 632, 475, and 774 cm^{-1}, which correspond to mode A_{1g}, bands S_2 and S_3, and 1350 cm^{-1} correspond to E_{2g} for SnO_2 and h-BN, respectively.[41,42]

For Li-S batteries, the separator's thermal stability is thought to be crucial. The thermal stability of the modified separators and pristine polypropylene separator was investigated by heating at 100 °C in air for 1 hour (Fig. S2, ESI†). As shown in Fig. S2 (ESI†), the shrinkage of the modified separators (Fig. S2a–c, ESI†) was much lower than that of the polypropylene separator

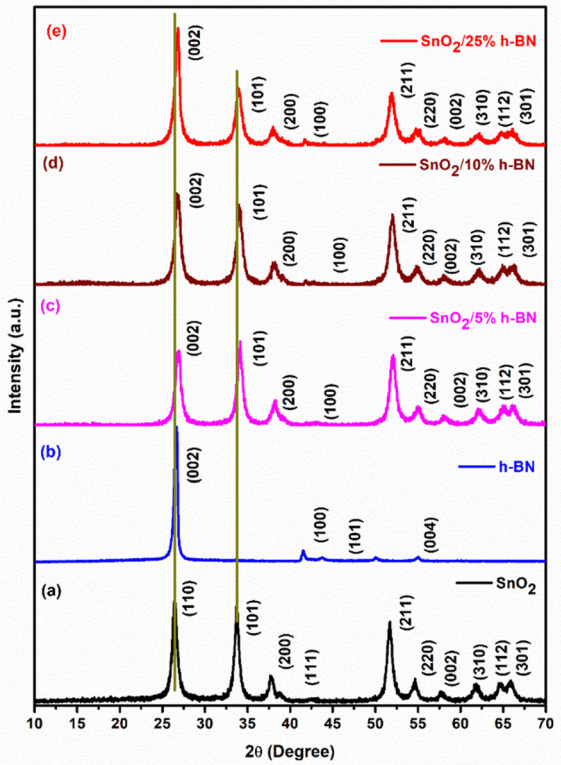

Fig. 1 XRD patterns of (a) SnO_2, (b) h-BN, (c) SnO_2/5% h-BN, (d) SnO_2/10% h-BN and (e) SnO_2/25% h-BN composites.

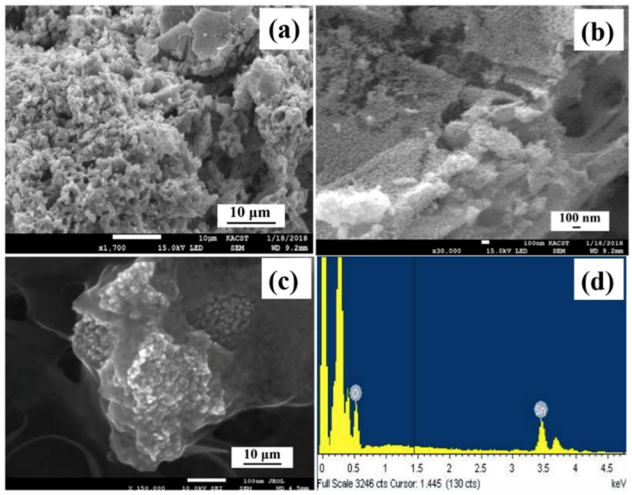

Fig. 2 (a) and (b) SEM images of pure SnO_2, (c) SEM and (d) EDX of the SnO_2/10% h-BN nanocomposite.

(Fig. S2d, ESI†) (Table S1, ESI†). Under this harsh condition, SnO_2/10% h-BN and SnO_2/25% h-BN composite modified separators show negligible thermal shrinkage. The significantly suppressed thermal shrinkage of the composite modified polypropylene separators is due to the anomalous characteristics of h-BN and SnO_2 and percentage of h-BN. The electrolyte penetration property of the SnO_2/h-BN modified separators was compared by single-droplet experiment using an electrolyte containing 1.0 wt% of $LiNO_3$, and 1,2-dimethoxyethane (DMC) and DOL in a volume ratio of 1 : 1 (Fig. S3, ESI†). The contact angle of the SnO_2/5% h-BN, SnO_2/10% h-BN and SnO_2/25% h-BN composite modified separators was 126.4°, 124.9° and 124.2°, respectively (Fig. S4, ESI†). The SnO_2/10% h-BN separator was fully wetted with the electrolyte due to its contact angle being less than that of the SnO_2/5% h-BN separator. The SnO_2/10% h-BN and SnO_2/25% h-BN coated separators show an almost similar contact angle as the separators quickly absorb the electrolyte droplet. The rate capability and cycling stability of LSBs could be considerably enhanced due to the good wettability and high electrolyte uptake, which could also minimize the electrolyte filling time and facilitate Li-ion migration.

Scanning electron microscopy (SEM) (Fig. 2) was used to take images of the final product, SnO_2/10% h-BN, in order to analyze the shape and particle size of SnO_2. Low magnification pictures of SnO_2 are shown in Fig. 2a, where nanoparticles of more or less homogeneous size and shape can be seen. High-magnification pictures of SnO_2 in Fig. 2b show the development of symmetrical, distinct nanoparticles that range in size from around 20 to 30 nm which is in agreement with the findings from transmission electron microscopy. High magnification SEM pictures of the SnO_2/10% h-BN composite are shown in Fig. 2c. The image clearly shows that SnO_2 nanoparticles have an h-BN coating, and TEM studies confirmed this. The energy dispersive X-ray (EDX) spectrum of the SnO_2/10% h-BN composite is shown in Fig. 2d. Based on the EDX measurement results, the SnO_2/10% h-BN nanocomposite consists of Sn, O, B and N elements. The atomic percentage of Sn, O, B, and N in the SnO_2/10% h-BN composite was 26.5, 52.1, 10.5, and 10.9, respectively.

Transmission electron microscopy (TEM) was used to further explore the architecture of SnO_2. Fig. S5a and b (ESI†) show the presence of SnO_2 nanoparticles in pristine SnO_2 which are in good agreement with the SEM images and range in size from 20 to 30 nm. Fig. 3 illustrates the HRTEM images of the SnO2/10% h-BN composite. SnO_2 nanoparticles and clusters are uniformly distributed over the layers of h-BN (Fig. 3a and c). It is really intriguing that many SnO_2 nanoparticles are trapped and positioned in a single h-BN sheet like peas in a pod as opposed to generating conformal layers on individual particles. A distinct confinement with h-BN can be seen in the HRTEM image of a single particle (SnO_2), which is better for conversion reactions (Fig. 3d). In accordance with the calculated XRD value, it also exhibits the presence of distinct lattice fringes with a *d*-spacing value of 0.34 nm, which is assigned to the (100) lattice plane of tetragonal SnO_2 (Fig. 3e). The SEAD pattern of the SnO_2/10% h-BN nanocomposite, shown in the inset of Fig. 3e, shows that the nanoparticles are irregular and polycrystalline in nature. A HRTEM image of the SnO_2/10% h-BN composite is shown in Fig. 3f, together with the appropriate elemental mapping (Fig. 3g–j). The SnO_2 nanocrystals are uniformly adorned on the h-BN nanosheets, according to the homogeneous distribution of boron, nitrogen, tin, and oxygen elements.

5.2. Electrochemical characterization

Fig. 4 displays the electrochemical performance of the Li–S cells created by utilizing the modified SnO_2/h-BN separators.

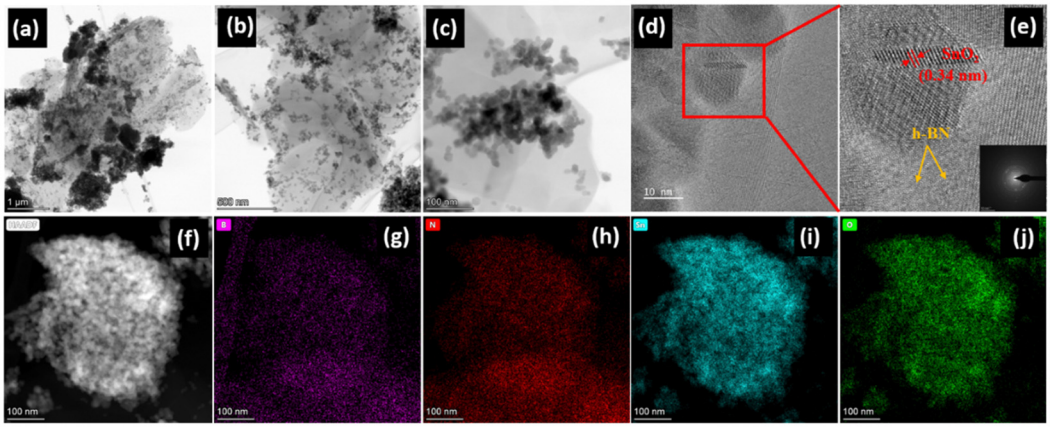

Fig. 3 (a–c) TEM images of SnO_2/10% h-BN, (d) HRTEM image, and (e) SAED of SnO_2/10% h-BN (bright field); (f) TEM image and the corresponding (g) boron, (h) nitrogen, (i) tin, and (j) oxygen EDX elemental mappings of a SnO_2/10% h-BN particle.

Elemental sulfur, carbon, and binder are simply combined to create the sulfur cathodes. Two cathodic peaks can be seen in Fig. 4a in the CV curves collected at 0.05 mV s^{-1}, which are attributed to the transformation of sulfur into soluble high-order polysulfides (Li_2S_x, $x \geq 4$) and the subsequent production of solid short-chain Li_2S/Li_2S_2. The peak at 2.43 results from the oxidation process of insoluble Li_2S_2/Li_2S to soluble Li_2S_x ($4 \leq x \leq 8$) and then to elemental sulfur.[43] Comparison of the CV curves of the SnO_2/10% h-BN separator cell to those of the SnO_2/5% h-BN and SnO_2/25% h-BN separator cells reveals a distinct change in the redox peaks. In contrast to the SnO_2/25% h-BN separator cell and nearly identical to the SnO_2/5% h-BN separator cell, the two reduction peaks of the SnO_2/10% h-BN separator cell are clearly visible at 2.01 V and 2.26 V (Fig. S5, ESI†). The oxidation peak of the SnO_2/10% h-BN separator is located at 2.42 V; this value is lower than the SnO_2/25% h-BN separator value (2.44 V) and nearly identical to the SnO_2/5% h-BN separator value (2.41 V). This demonstrates that the SnO_2/10% h-BN separator shows faster redox reactions.[44] The peak current density of the SnO_2/10% h-BN separator cell differs from that of the SnO_2/5% h-BN and SnO_2/25% h-BN separator cells, clearly indicating a change in capacity even if the forms of the CV curves are unchanged. Fig. 4 b shows the CV curves of the five initial cycles of the SnO_2/10% h-BN separator at a scan rate of 0.1 mV s^{-1} and it can be observed that the current response and peak positions are superimposed, which indicates the excellent reversibility of the SnO_2/10% h-BN separator with sulfur cathode.

For the actual uses of LSBs, long-term cycle stability is essential. Fig. 4c and Fig. S7 (ESI†) show the evaluation of the long-cycling stability of SnO_2/5% h-BN, SnO_2/10% h-BN, SnO_2/15% h-BN, SnO_2/20% h-BN and SnO_2/25% h-BN modified separator cells. SnO_2/5% h-BN, SnO_2/10% h-BN, and SnO_2/25% h-BN modified separator cells have initial discharge capacities of 414, 620, and 353 mA h g^{-1} at 1C, respectively. SnO_2/10% h-BN delivered a high reversible capacity of 485 mA h g^{-1} after cycling for 350 cycles, whereas SnO_2/5% h-BN, SnO_2/15% h-BN, SnO_2/20% h-BN and SnO_2/25% h-BN modified separator cells delivered 325, 250, 190 and 184 mA h g^{-1}, respectively. The capacity of SnO_2/10% h-BN is 1.5, 1.9, 2.5 and 2.6 times higher than that of SnO_2/5% h-BN, SnO_2/15% h-BN, SnO_2/20% h-BN and SnO_2/25% h-BN modified separator cells even after 350 cycles, respectively. The coulombic efficiency, initially and after 350 cycles, of the SnO_2/5% h-BN, SnO_2/10% h-BN, SnO_2/15% h-BN, SnO_2/20% h-BN and SnO_2/25% h-BN modified separator cells was 86, 89, 87, 80 and 91% and 91, 99, 83, 86 and 95%, respectively. Even after 350 cycles, the capacity of the SnO_2/10% h-BN-modified separator remains stable, suggesting outstanding cycling stability brought on by polysulfide inhibition during charge–discharge cycling. Particularly, the coulombic efficiency of the Li–S cell was increased by the SnO_2/10% h-BN modified separator to 99% (after 350 cycles) as a result of the significant reduction in LiPS migration caused by physical and chemical interactions between the modified separator and the dissolved LiPSs. Variations in electrode resistance and changes in carbon surface area during a cycle may be blamed for the observed fluctuations in cell capacity values and coulombic efficiency.[45] The areal capacity of the SnO_2/10% h-BN (0.4 mA h cm^{-2}) modified separator was higher than that of the SnO_2/5% h-BN (0.2 mA h cm^{-2}) and SnO_2/25% h-BN (0.16 mA h cm^{-2}) modified separators after 350 cycles (Fig. S8, ESI†). These effects cause changes in the way that polysulfides react with lithium ions, which modifies how sulfur is used up throughout each cycle.

Fig. 4d displays the charge–discharge voltage profiles for the Li–S cells constructed from the pristine separator (polypropylene, PP) and the SnO_2-modified separators, both recorded at a rate of 1C. It is evident that sulfur redox reactions between sulfur and polysulfides are taking place because the entire plateau for charge–discharge operations precisely corresponds to the peak positions of the CV curves. The charge curve contains one peak for the oxidation of lower-order lithium-polysulfides (LLPS) to elemental sulfur, which is in agreement with the CV observations, whereas the discharge curve mostly consists of two plateaus attributed to the creation of higher-order lithium-polysulfides (HLPS) followed by subsequent reduction to LLPS. It is interesting to note that for both unaltered and altered separator cells, a difference in the voltage

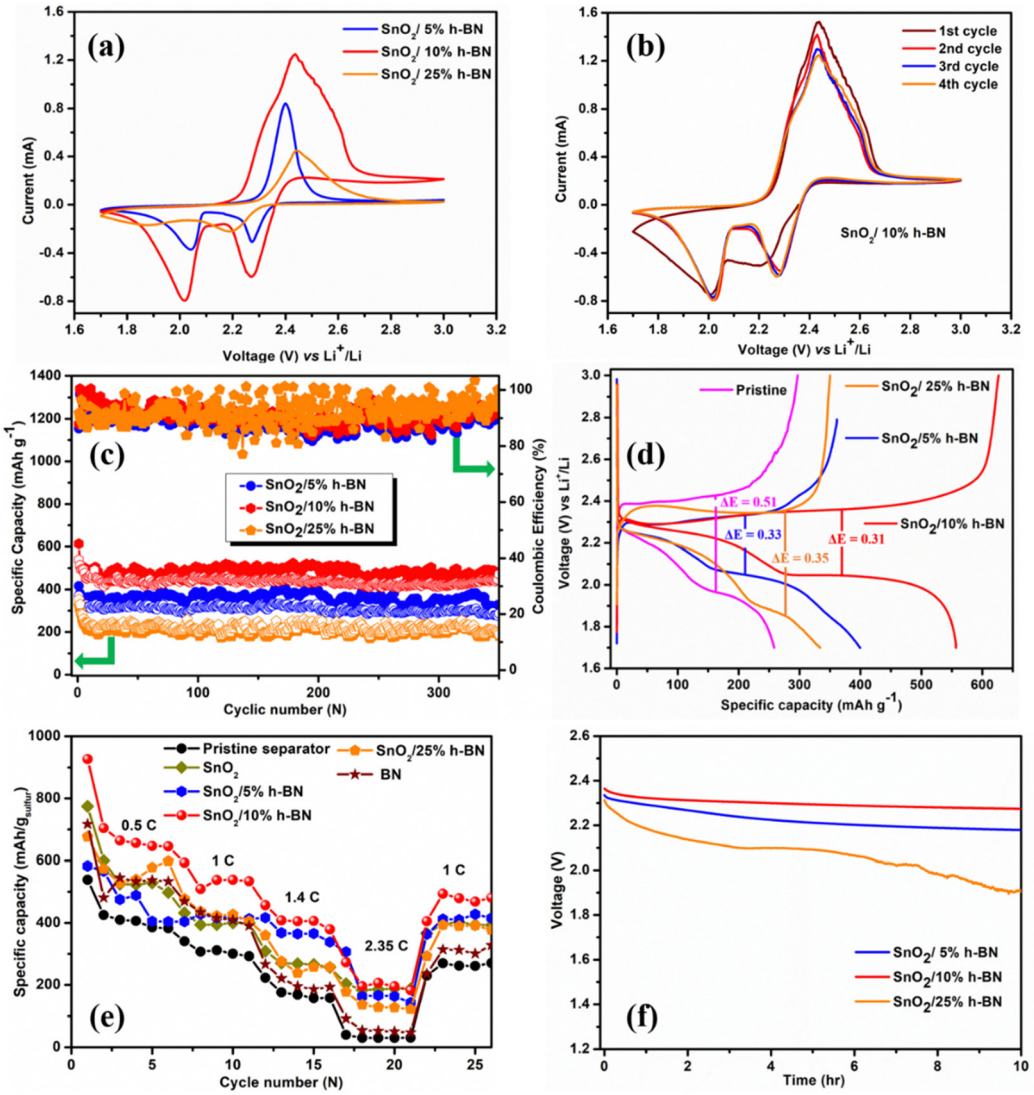

Fig. 4 Electrochemical performance: (a) CV curves of SnO_2/5% h-BN, SnO_2/10% h-BN and SnO_2/25% h-BN composites, (b) CV curves of SnO_2/10% h-BN (1 to 4 cycles), (c) cycling performance with the modified separator at a current rate of 1.0C, (d) discharge/charge in the first cycle of the Li–S cell with the modified separator at a current rate of 1.0C. (e) Rate capability behaviour of the Li–S cell with the modified separator, (f) potential variation with time for open-circuit potential (OCP) of SnO_2/5% h-BN, SnO_2/10% h-BN and SnO_2/25% h-BN.

hysteresis is seen for charging and discharging at average capacity. The Li–S cell with a SnO_2/h-BN modified separator has a larger initial discharge capacity, which indicates that the active material is used more effectively in the cell. The SnO_2/h-BN modified separators' ability to effectively prevent polysulfide migration and to reawaken imprisoned polysulfides has therefore been thoroughly proven. The PP separator cell exhibited a higher voltage hysteresis value (0.51 V) compared to the altered separator cells. These results demonstrated that the SnO_2/h-BN interlayer could reduce the polarization in the Li–S cell due to the abundant catalytic sites chemically bind with LiPSs, which is in agreement with the CV results. It is significant to highlight that in the SnO_2/5% h-BN composite, h-BN nanosheets at extremely low concentrations on polymer membranes would not be able to completely adsorb the dissolved polysulfide species. On the other hand, an excessive concentration of h-BN in the SnO_2/25% h-BN composite may cause the cell's internal resistance to increase due to the insulated nature of h-BN. Therefore, SnO_2/10% h-BN nanosheet concentration optimization is essential to achieve desired polysulfide adsorption characteristics and thereby prevent polysulfides from reaching the metallic lithium anode. A SnO_2/10% h-BN concentration was found to be optimal with the least amount of polarization after rigorous examination of polarization (the difference between discharge and charge plateau potential). Such behaviour was a sign that the newly improved separator was suitable for extensive Li–S battery cycling.

The rate performance of Li–S cells constructed from SnO_2, h-BN, and SnO_2/h-BN (5, 10 and 25%) composite modified separators and the pristine separator was studied at various C rates ranging from 0.5 to 2.3 5C in order to investigate the benefit of the SnO_2/h-BN modified separator and its viability for practical use (Fig. 4e). Surprisingly, the SnO_2/10% h-BN

modified separator outperformed the other compositions, namely, SnO_2, h-BN, and PP separator, in terms of capacity at each current rate. While this was happening, the capacity of the SnO_2/10% h-BN modified separator was reduced when it was cycled back after being used at higher current rates. This demonstrates the ability of the SnO_2/10% h-BN modified separator to function at a varied current rate in accordance with the user's requirements. The discharge capacities of the SnO_2/10% h-BN modified separator cell were found to be 928, 648, 535 and 381 mA h g^{-1} at C rates of 0.5, 1.0, 1.4 and 2.35, respectively.

In general, the Li-S batteries degrade over time due to the self-discharge, which is due to the negatively charged intermediate species. In addition, those species have a tendency to drift away from the cathode due to rising electrostatic attraction forces of the metallic lithium anode.[46–48] The open circuit potential (OCP), which was measured for 10 hours and is shown in Fig. 4f, was used to quantify the self-discharge action of LSBs with SnO_2/5% h-BN, SnO_2/10% h-BN, and SnO_2/25% h-BN modified separators. It is interesting to note that the cell with a separator modified with SnO_2/10% h-BN stabilized in 1 hour with an OCP of 2.35 V and maintained this OCP for 10 hours. In contrast, a persistent decrease in OCP was seen in the cells using the modified separators SnO_2/5% h-BN and SnO_2/25% h-BN. SnO_2 and enough polar-natured h-BN nanosheets are responsible for the cell's ability to prevent the dissolution of sulfur at the electrode–electrolyte interface.

The post-mortem analysis was carried out in the discharge state after 350 cycles at 1C to better understand the function of the SnO_2/10% h-BN modified separator in the electrochemical reaction. Fig. 5 illustrates that while the surface of the lithium metal was not coloured by polysulfides with the SnO_2/10% h-BN (Fig. 5b) separator, that of the SnO_2/5% h-BN and SnO_2/25% h-BN separators approaching the Li anode is painted with yellow colour as a result of the migration of polysulfides through these separators. This indicates that SnO_2/10% h-BN has a stronger adsorption effect on polysulfides compared to SnO_2/5% h-BN and SnO_2/25% h-BN composites. The occurrence suggests that boron nitride in the composite is the primary source of adsorption, and that the synergistic interaction between h-BN and SnO_2 can considerably increase this adsorption. We created the polysulfide diffusion test bottles as shown in Fig. S9 (ESI†) to confirm the impact of the SnO_2/10% h-BN composite on inhibiting the diffusion of polysulfides through the membrane. To determine which separator controls the rate of polysulfide diffusion, three diffusion test bottles were created by utilizing SnO_2/5% h-BN, SnO_2/10% h-BN, and SnO_2/25% h-BN separators. SnO_2/5% h-BN (Fig. S9a, ESI†) and SnO_2/25% h-BN (Fig. S9c, ESI†) separators were unable to hold the polysulfides for a longer period and allowed the diffusion of the polysulfides to the bottom side vial in 24 hours (yellow color). However, the SnO_2/10% h-BN separator was able to control the diffusion of polysulfides to the bottom side vial for 24 hours. This demonstrates the SnO_2/10% h-BN separator's ability to stop the migration of polysulfides to the lithium anode. The polysulfide solution that was collected from the bottom side of the vial was also subjected to UV-Vis spectroscopy in order to confirm the effectiveness of the SnO_2/5% h-BN, SnO_2/10% h-BN, and SnO_2/25% h-BN separators. Fig. S9d (ESI†) displays the UV-Vis spectra for SnO_2/5% h-BN, SnO_2/10% h-BN, and SnO_2/25% h-BN. Two separate peaks at 238 nm and 261 nm wavelengths were seen in the UV-Vis spectra. These two peaks can be assigned to the presence of polysulfides (Li_2S_8 and Li_2S_6). Because of the polysulfides' diffusion to the vial's bottom side, as seen in Fig. S9d (ESI†), the SnO_2/10% h-BN separator had a lower peak intensity than the SnO_2/5% h-BN and SnO_2/25% h-BN separators. This study clearly shows the ability of the SnO_2/10% h-BN separator to hold and mitigate the migration of polysulfides.

6. Conclusions

In conclusion, BN nanosheet composites supported by SnO_2 were successfully created. To recommend SnO_2/ h-BN as a better-performing separator, the ideal concentration of 10wt% h-BN and with the existence of micro/nanostructure so as to admit the polysulfides, this synergy can reduced the resistance in transporting the lithium ions easily. The good capacity retention for 350 cycles at 1C rate was realized through extensive electrochemical experiments. More crucially, after 10 hours, the rate of self-discharge for the SnO_2/10% h-BN modified separator cell was virtually non-existent, in contrast to the substantial

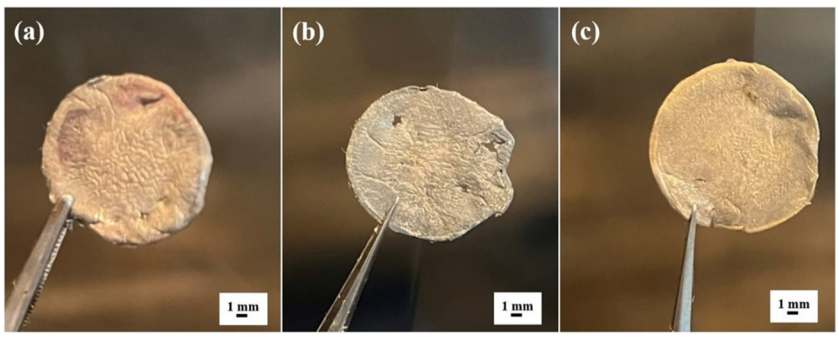

Fig. 5 Digital photograph of the lithium metal anodes after 350 charge/discharge cycles at 1C rate: (a) lithium anode with the SnO_2/5% h-BN composite separator, (b) lithium anode with the SnO_2/10% h-BN composite separator and (c) lithium anode with the SnO_2/25% h-BN composite separator.

self-discharge rates for the SnO_2/5% h-BN and SnO_2/25% h-BN modified separator-based cells. It was expected that a polar natured separator would strongly promote polysulfide adsorption without allowing them to cross over to metallic lithium.

Conflicts of interest

On behalf of all authors, the corresponding author states that there is no conflict of interest.

Acknowledgements

This work is part of a research project in collaboration with EXPEC Advanced Research Center, Saudi Aramco, under agreement no. AFU-01-2017. The authors gratefully acknowledge Alfaisal University and its Office of Research for their continuous support throughout this study.

References

1 A. Manthiram, Y. Fu, S.-H. Chung, C. Zu and Y.-S. Su, *Chem. Rev.*, 2014, **114**, 11751–11787.
2 P. G. Bruce, S. A. Freunberger, L. J. Hardwick and J.-M. Tarascon, *Nat. Mater.*, 2012, **11**, 19–29.
3 D. Liu, C. Zhang, G. Zhou, W. Lv, G. Ling, L. Zhi and Q. Yang, *Adv. Sci.*, 2018, **5**, 1700270.
4 N. Xu, T. Qian, X. Liu, J. Liu, Y. Chen and C. Yan, *Nano Lett.*, 2017, **17**, 538–543.
5 Y. Sun, Z. W. Seh, W. Li, H. Yao, G. Zheng and Y. Cui, *Nano Energy*, 2015, **11**, 579–586.
6 Q. Pang, A. Shyamsunder, B. Narayanan, C. Y. Kwok, L. A. Curtiss and L. F. Nazar, *Nat. Energy*, 2018, **3**, 783–791.
7 X. Liu, J.-Q. Huang, Q. Zhang and L. Mai, *Adv. Mater.*, 2017, **29**, 1601759.
8 W. Chen, T. Lei, C. Wu, M. Deng, C. Gong, K. Hu, Y. Ma, L. Dai, W. Lv and W. He, *Adv. Energy Mater.*, 2018, **8**, 1702348.
9 N. Jayaprakash, J. Shen, S. S. Moganty, A. Corona and L. A. Archer, *Angew. Chem.*, 2011, **123**, 6026–6030.
10 J. Kim, D. Lee, H. Jung, Y. Sun, J. Hassoun and B. Scrosati, *Adv. Funct. Mater.*, 2013, **23**, 1076–1080.
11 C. Hoffmann, S. Thieme, J. Brückner, M. Oschatz, T. Biemelt, G. Mondin, H. Althues and S. Kaskel, *ACS Nano*, 2014, **8**, 12130–12140.
12 X. Ji, K. T. Lee and L. F. Nazar, *Nat. Mater.*, 2009, **8**, 500–506.
13 Z. Li, Y. Jiang, L. Yuan, Z. Yi, C. Wu, Y. Liu, P. Strasser and Y. Huang, *ACS Nano*, 2014, **8**, 9295–9303.
14 X. Yang, L. Zhang, F. Zhang, Y. Huang and Y. Chen, *ACS Nano*, 2014, **8**, 5208–5215.
15 R. Fang, S. Zhao, S. Pei, X. Qian, P.-X. Hou, H.-M. Cheng, C. Liu and F. Li, *ACS Nano*, 2016, **10**, 8676–8682.
16 Z. Wei Seh, W. Li, J. J. Cha, G. Zheng, Y. Yang, M. T. McDowell, P.-C. Hsu and Y. Cui, *Nat. Commun.*, 2013, **4**, 1331.
17 P. Zeng, L. Huang, X. Zhang, Y. Han and Y. Chen, *Appl. Surf. Sci.*, 2018, **427**, 242–252.
18 C.-H. Chang, S.-H. Chung and A. Manthiram, *J. Mater. Chem. A*, 2015, **3**, 18829–18834.
19 H. Ye, Y.-X. Yin, S. Xin and Y.-G. Guo, *J. Mater. Chem. A*, 2013, **1**, 6602–6608.
20 Z. Wang, Y. Dong, H. Li, Z. Zhao, H. Bin Wu, C. Hao, S. Liu, J. Qiu and X. W. D. Lou, *Nat. Commun.*, 2014, **5**, 1–8.
21 N. Li, M. Zheng, H. Lu, Z. Hu, C. Shen, X. Chang, G. Ji, J. Cao and Y. Shi, *Chem. Commun.*, 2012, **48**, 4106–4108.
22 X. Jia, C. Zhang, J. Liu, W. Lv, D.-W. Wang, Y. Tao, Z. Li, X. Zheng, J.-S. Yu and Q.-H. Yang, *Nanoscale*, 2016, **8**, 4447–4451.
23 J.-Q. Huang, T.-Z. Zhuang, Q. Zhang, H.-J. Peng, C.-M. Chen and F. Wei, *ACS Nano*, 2015, **9**, 3002–3011.
24 L. Zhu, H.-J. Peng, J. Liang, J.-Q. Huang, C.-M. Chen, X. Guo, W. Zhu, P. Li and Q. Zhang, *Nano Energy*, 2015, **11**, 746–755.
25 J.-Q. Huang, H.-J. Peng, X.-Y. Liu, J.-Q. Nie, X.-B. Cheng, Q. Zhang and F. Wei, *J. Mater. Chem. A*, 2014, **2**, 10869–10875.
26 H. Li, X. Yang, X. Wang, Y.-S. He, F. Ye, M. Liu and Y. Zhang, *Nanoscale*, 2016, **8**, 2395–2402.
27 G. Ma, Z. Wen, J. Jin, Y. Lu, X. Wu, M. Wu and C. Chen, *J. Mater. Chem. A*, 2014, **2**, 10350–10354.
28 Y. Dong, S. Liu, Z. Wang, Y. Liu, Z. Zhao and J. Qiu, *Nanoscale*, 2015, **7**, 7569–7573.
29 S. Chung and A. Manthiram, *Adv. Mater.*, 2014, **26**, 1360–1365.
30 Q. Pang, D. Kundu, M. Cuisinier and L. Nazar, *Nat. Commun.*, 2014, **5**, 1–8.
31 X. Liang, C. Hart, Q. Pang, A. Garsuch, T. Weiss and L. F. Nazar, *Nat. Commun.*, 2015, **6**, 1–8.
32 H. Yao, G. Zheng, P.-C. Hsu, D. Kong, J. J. Cha, W. Li, Z. W. Seh, M. T. McDowell, K. Yan and Z. Liang, *Nat. Commun.*, 2014, **5**, 1–9.
33 Z. Zhang, Y. Lai, Z. Zhang, K. Zhang and J. Li, *Electrochim. Acta*, 2014, **129**, 55–61.
34 Y. Yang, H. Xu, S. Wang, Y. Deng, X. Qin, X. Qin and G. Chen, *Electrochim. Acta*, 2019, **297**, 641–649.
35 B. Campbell, J. Bell, H. H. Bay, Z. Favors, R. Ionescu, C. S. Ozkan and M. Ozkan, *Nanoscale*, 2015, **7**, 7051–7055.
36 Y. Xiang, Z. Wang, W. Qiu, Z. Guo, D. Liu, D. Qu, Z. Xie, H. Tang and J. Li, *J. Membr. Sci.*, 2018, **563**, 380–387.
37 J. Liu, L. Yuan, K. Yuan, Z. Li, Z. Hao, J. Xiang and Y. Huang, *Nanoscale*, 2016, **8**, 13638–13645.
38 H. Ahn, Y. Kim, J. Bae, Y. K. Kim and W. B. Kim, *Chem. Eng. J.*, 2020, **401**, 126042.
39 W. Luo, L. Zhou, K. Fu, Z. Yang, J. Wan, M. Manno, Y. Yao, H. Zhu, B. Yang and L. Hu, *Nano Lett.*, 2015, **15**, 6149–6154.
40 M. F. Rodrigues, K. Kalaga, H. Gullapalli, G. Babu, A. L. M. Reddy and P. M. Ajayan, *Adv. Energy Mater.*, 2016, **6**, 1600218.
41 A. Dieguez, A. Romano-Rodrıguez, A. Vila and J. Morante, *J. Appl. Phys.*, 2001, **90**, 1550–1557.
42 D. H. Suh, *Nanoscale*, 2014, **6**, 5686–5690.
43 H. Tang, W. Li, L. Pan, C. P. Cullen, Y. Liu, A. Pakdel, D. Long, J. Yang, N. McEvoy and G. S. Duesberg, *Adv. Sci.*, 2018, **5**, 1800502.
44 F. Li, G. Hu, S. Li, C. Hou and J. Gao, *Electrochim. Acta*, 2020, **340**, 135991.

45 G. Babu, A. Sawas, N. K. Thangavel and L. M. R. Arava, *J. Phys. Chem. C*, 2018, **122**, 10765–10772.
46 L. Wang, J. Liu, S. Yuan, Y. Wang and Y. Xia, *Energy Environ. Sci.*, 2016, **9**, 224–231.
47 V. Knap, D.-I. Stroe, M. Swierczynski, R. Teodorescu and E. Schaltz, *J. Electrochem. Soc.*, 2016, **163**, A911.
48 H. Ryu, H. Ahn, K. Kim, J. Ahn, K. Cho and T. Nam, *Electrochim. Acta*, 2006, **52**, 1563–1566.